Supplementary Information

Skin-mimicking biogel-based iontronic sensor with hierarchical bionic coupling for dexterous tactile e-skin

Yidan Chen [1,†], Shu Wang [1,†], Xilu Ye [1,†], Chenghui Lv [1], Jialin Wei [1], Yingxin Zhang [1], Jianfeng Ping [1,2], Yibin Ying [1,2], Lingyi Lan [1,2]*

[1] College of Biosystems Engineering and Food Science, Zhejiang University, Hangzhou 310058, P.R. China.

[2] Zhejiang Key Laboratory of Intelligent Sensing and Robotics for Agriculture, Zhejiang University, Hangzhou 310058, P.R. China.

[†] These authors contributed equally: Yidan Chen, Shu Wang, Xilu Ye.

*Corresponding author: lingyilan@zju.edu.cn

Contents

Supplementary Notes

Supplementary Note 1. Theoretical analysis of measuring the elastic modulus of fruits by a texture analyzer.

Due to the fact that the stiffness of the metal probe in the texture analyzer is significantly greater than the elastic modulus of the fruit, and the diameter of the fruit exceeds the indentation depth of the probe, the Boussinesq model can be applied to calculate the fruit's elastic modulus. The elastic modulus (*E*) of the fruit is related to external force (*F*), indentation depth (*D*), probe radius (*R*), and Poisson's ratio (μ). The elastic modulus (*E*) can be expressed as the following equation:

$$E = \frac{F(1-\mu^2)}{4DR} \tag{S1}$$

Supplementary Note 2. Theoretical analysis of measuring the elastic modulus of fruits by sensing system.

Compared with the texture analysis method using a texture analyzer, the single-finger pressing process with a dexterous hand equipped with the hand-shaped iontronic sensor array involves distinct technical considerations. During this process, the sensor itself undergoes deformation, primarily due to the elastic properties of the biogel. When an external force (F) is applied, the total deformation (D_{total}) of the system can be expressed as the sum of the deformation (D_s) of the sensor at the fingertip and the deformation (D_f) of the fruit being measured:

$$D_{total} = D_s + D_f \qquad (S2)$$

The relationship between capacitance changes and system stress can be derived from the capacitance-stress variation curve of the sensor. The stress (P) in the system is defined as the ratio of the change in capacitance (ΔC) to the initial capacitance (C_0), divided by the sensitivity (S):

$$P = \frac{\Delta C / C_0}{S} \qquad (S3)$$

Using these foundational principles, the elastic modulus (E) can be calculated with the following equation:

$$E = \frac{\pi R \Delta C (1 - \mu^2)}{4 C_0 S (D_{total} - D_s)} \qquad (S4)$$

Sensor modulus, alongside sensitivity, is a critical parameter for measurement accuracy. As mentioned above, if the sensor is too compliant, its deformation becomes non-negligible, leading to an underestimation of the object's true modulus. On the other hand, if the sensor is made excessively stiff to minimize self-deformation, it may generate localized stress concentrations at the contact interface, potentially exceeding the bio-yield point of delicate fruits and causing mechanical damage. Thus, for nondestructive fruit modulus measurement, the sensor must balance two competing requirements: it should be stiff enough to ensure reliable mechanical readout, while still sufficiently compliant to maintain gentle, nondestructive contact.

Supplementary Figures

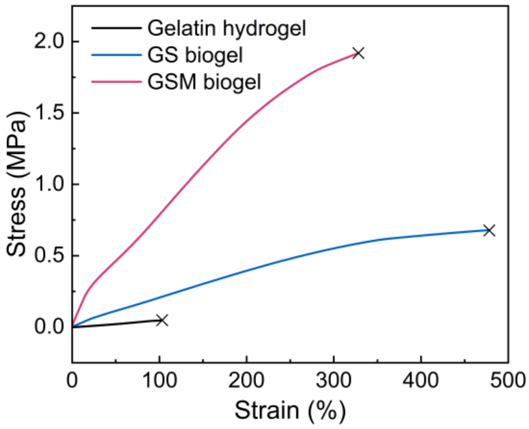

Supplementary Fig. 1. Stress-strain curves of gelatin hydrogel, GS biogel, and GSM biogel. It was found that the addition of SL enhanced the stretchability and toughness of the biogel, and the subsequent incorporation of MMT further improved its toughness.

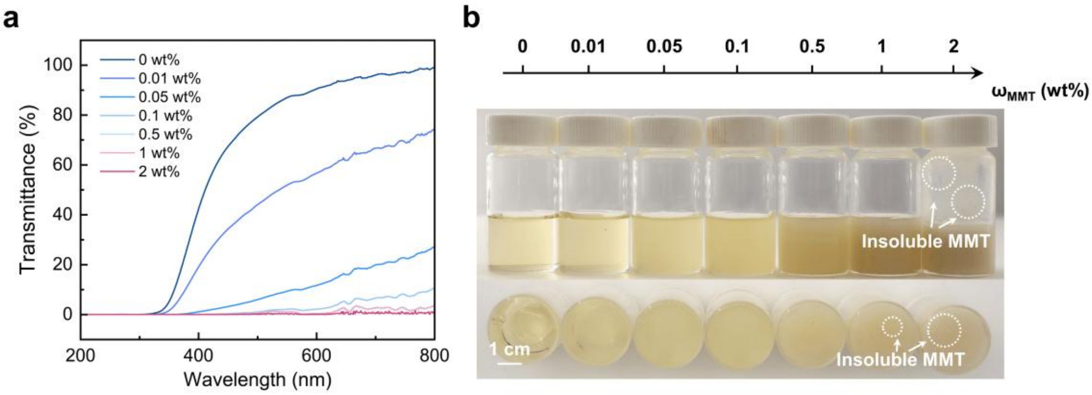

Supplementary Fig. 2. The influence of different MMT weight ratios on the light transmittance. a, UV–visible spectra revealed that the sample without MMT exhibited relatively lower transmittance at shorter wavelengths and higher transmittance at longer wavelengths, which was attributed to the absorption of blue-violet light by the pale-yellow gelatin solution. As the MMT concentration increased, the transmittance of the samples gradually decreased across the entire visible spectrum. b, Photographs showed that with increasing MMT concentration, the samples gradually became more opaque. Scale bar, 1 cm.

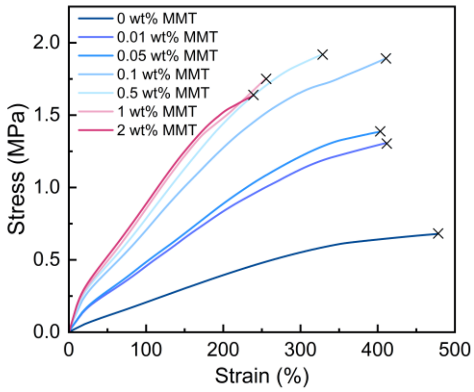

Supplementary Fig. 3. Stress-strain curves of GSM biogel with different MMT weight ratios.

It was found that as the MMT content increased, the fracture stress of the biogel gradually increased.

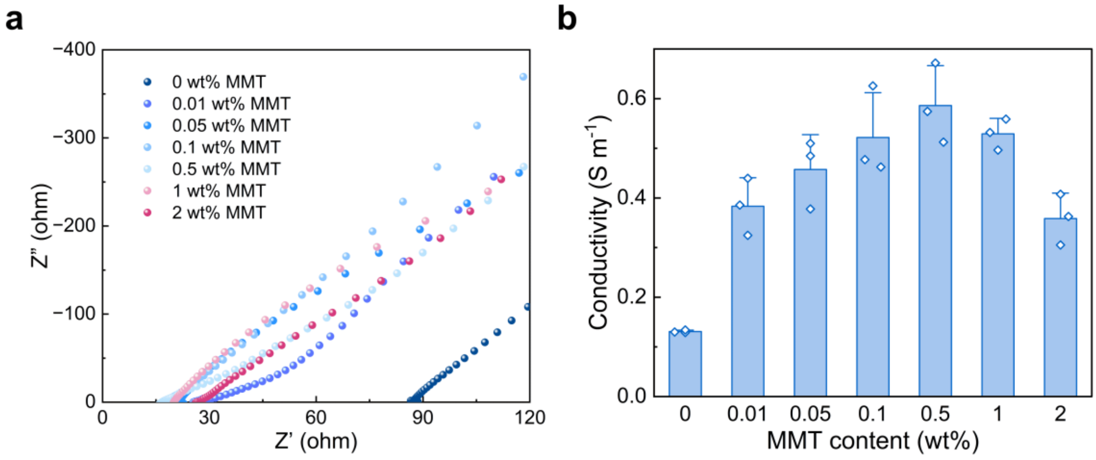

Supplementary Fig. 4. The influence of different MMT weight ratios on the ionic conductivity of biogel. a, Impedance spectroscopy revealed that the x-axis intercept, representing the biogel resistance, gradually decreased with increasing MMT content. b, The addition of MMT increased the conductivity of the GSM biogel. Data were presented as mean values +/- SD, n=3.

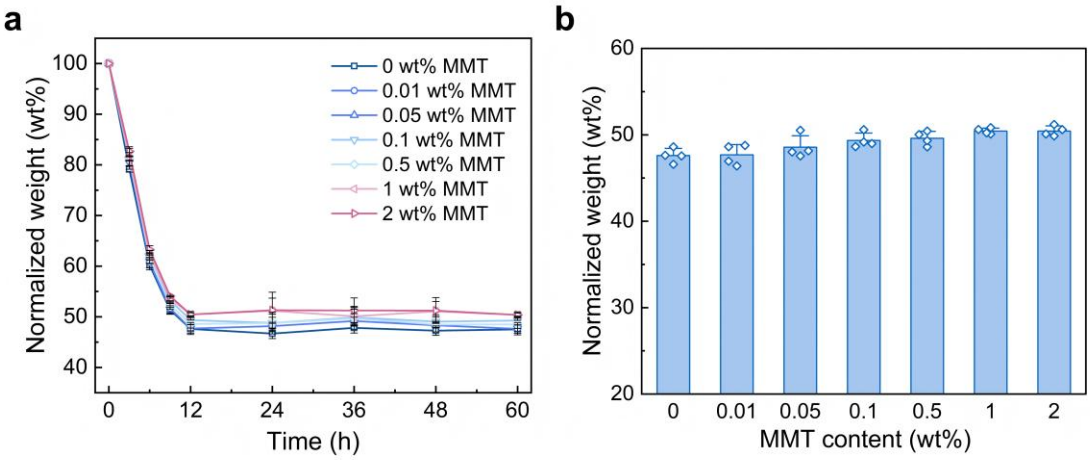

Supplementary Fig. 5. The influence of different MMT weight ratios on the water retention of biogel. a, The variation of normalized weight under different storage times. b, The final normalized weight after water stability of GSM biogel with different MMT weight ratios. It was found that the normalized weight of the GSM biogel reached equilibrium after 12 hours of storage, and that the addition of MMT had little effect on the biogel normalized weight. Data were presented as mean values +/- SD, n=4.

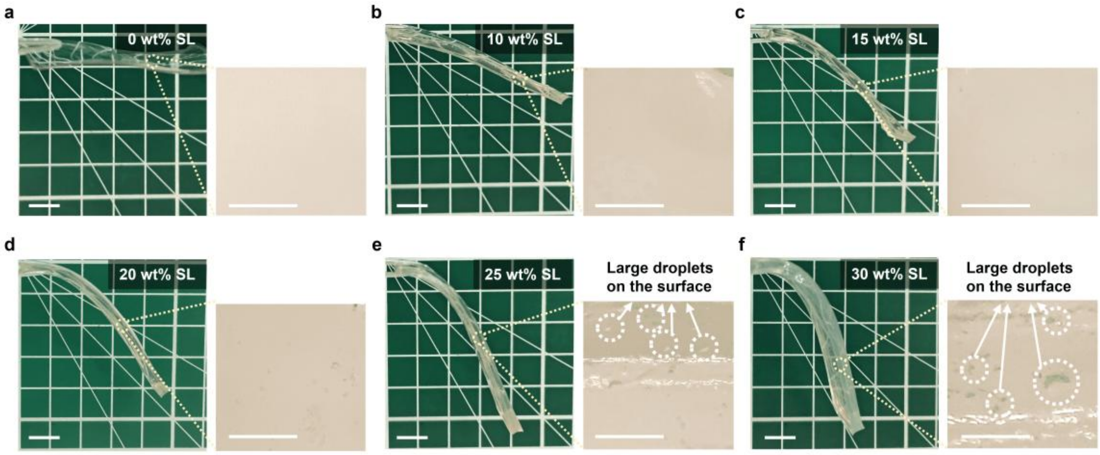

Supplementary Fig. 6. The influence of different SL weight ratios on the appearance of biogel. The side and surface enlarged photographs of GS biogel with a, 0 wt%, b, 10 wt%, c, 15 wt%, d, 20 wt%, e, 25 wt%, f, 30 wt% SL. These photographs showed that the addition of SL gradually increased the softness and hydrophilicity of the biogel. When the SL concentration reached 25 wt%, droplets began to appear on the biogel surface. Scale bars, 1 cm.

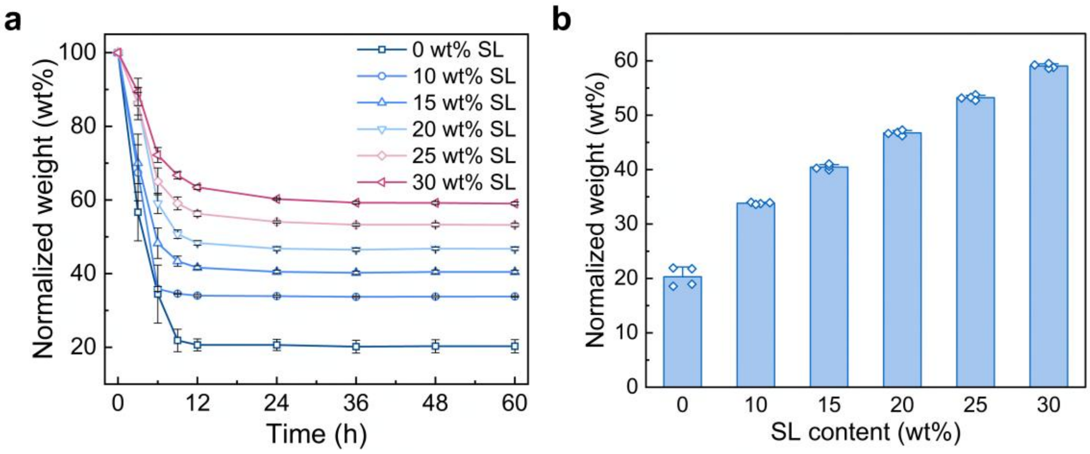

Supplementary Fig. 7. The influence of different SL weight ratios on the water retention of biogel. a, The variation of normalized weight under different storage times. b, The final normalized weight after water stability of GS biogel with different SL weight ratios. It was found that the normalized weight of the GSM biogel reached equilibrium after 12 hours of storage, and that the addition of SL increased the biogel normalized weight. Data were presented as mean values +/- SD, n=4.

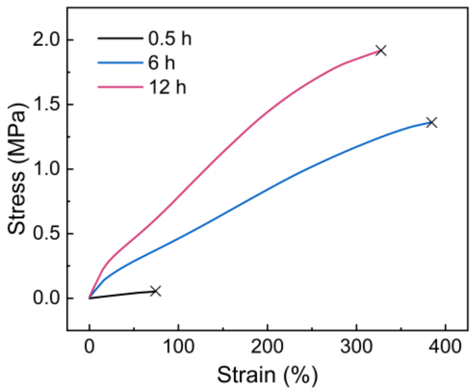

Supplementary Fig. 8. Stress-strain curves of GSM biogel under different storage times. It was found that as the storage time increased, the fracture stress of the GSM biogel gradually increased.

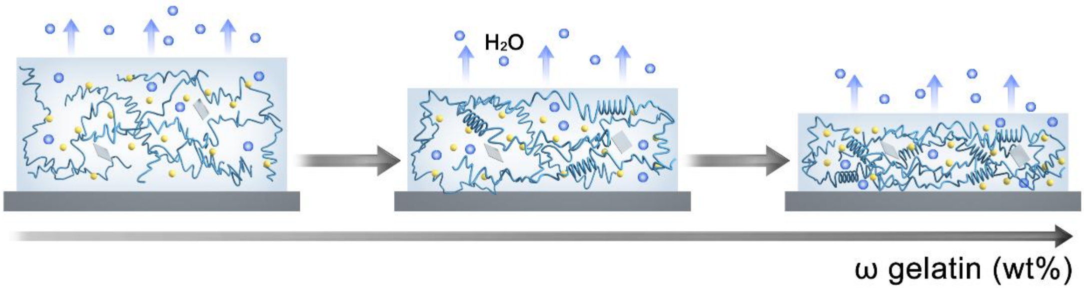

Supplementary Fig. 9. Schematic diagram of the internal network changes of the GSM biogel with the extension of storage time. This schematic illustrated the evolution of the internal molecular structure of the GSM biogel during the equilibration process. At the initial stage, the system mainly consisted of short-chain gelatin polypeptides after cooling, with a high water content. The interactions between polymer chains and free water molecules dominated, and the biogel macroscopically appeared soft and fragile. As equilibration proceeded, the biogel gradually lost water, and the solvation effect diminished. The interactions between polymer chains and water molecules weakened, while single gelatin chains progressively self-assembled into triple helices, accompanied by enhanced electrostatic interactions and hydrogen bonding with sodium lactate and MMT. When the biogel finally reached hydration equilibrium, due to the strong affinity of sodium lactate for water molecules, most of the water in the system existed as bound water, with free water substantially reduced. At this stage, the network compactness and toughness of the GSM biogel reached their maximum.

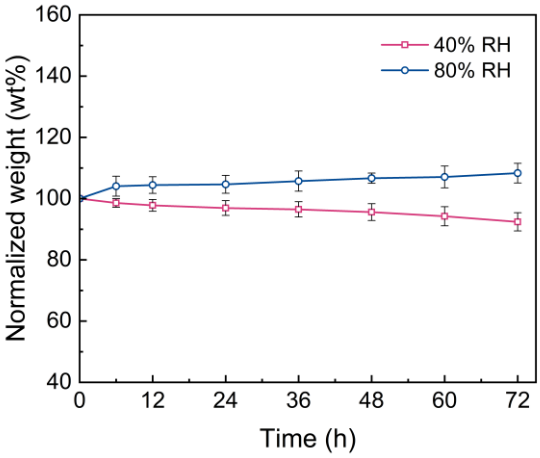

Supplementary Fig. 10. The hydration stability of biogel under different humidity (40% RH and 80% RH). It was found that the biogel weight increased to 110% at 80% RH and decreased to 94% at 40% RH after 72 h, reflecting the intrinsic hygroscopic nature of SL within the network. Data were presented as mean values +/- SD, n=3.

a

b

Supplementary Fig. 11. Photographs showing the stretchability of the GSM biogel. a, Photographs of the GSM biogel before stretching. b, Photographs of the GSM biogel after stretching.

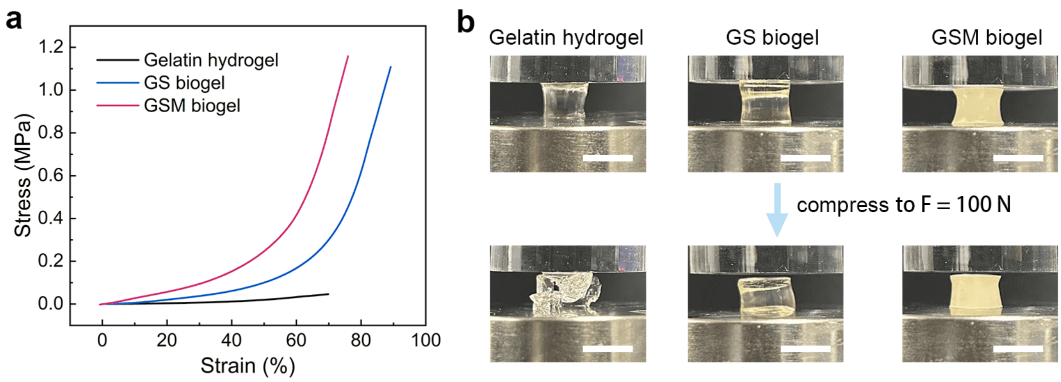

Supplementary Fig. 12. Compressive properties of different biogels. a, Compressive stress-strain curves of gelatin hydrogel, GS biogel, and GSM biogel. b, Photographs of gelatin hydrogel, GS biogel, and GSM biogel before and after compression. It was found that the addition of SL and MMT increased the compressive modulus of the biogel, and the GSM biogel maintained good integrity under an external force of 100 N. Scale bars, 1 cm.

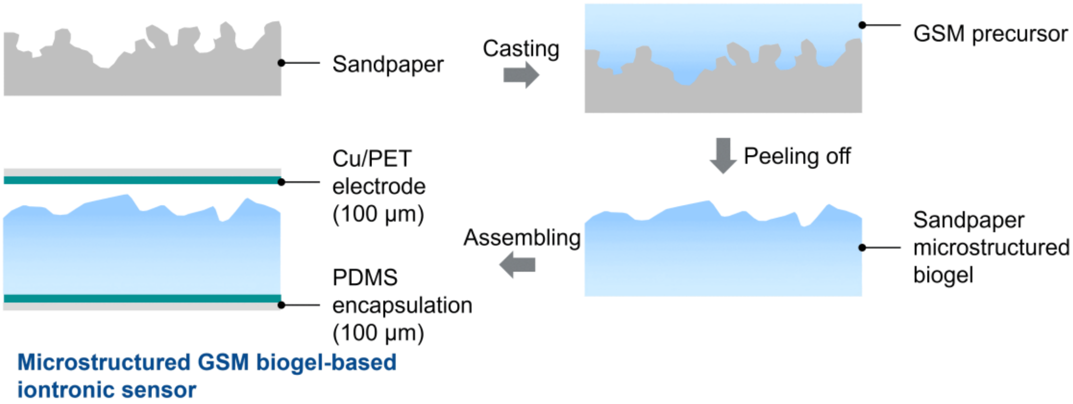

Supplementary Fig. 13. Schematic diagram of an assembly microstructured GSM biogel-based iontronic sensor. The microstructured GSM biogel was fabricated by injecting the precursor solution into a glass reaction cell containing 5000# sandpaper as a template, followed by gelation upon cooling. This microstructured biogel was then sandwiched between two 100 μm thick Cu/PET electrodes and encapsulated with a 100 μm thick PDMS layer, yielding a microstructured GSM biogel-based iontronic sensor.

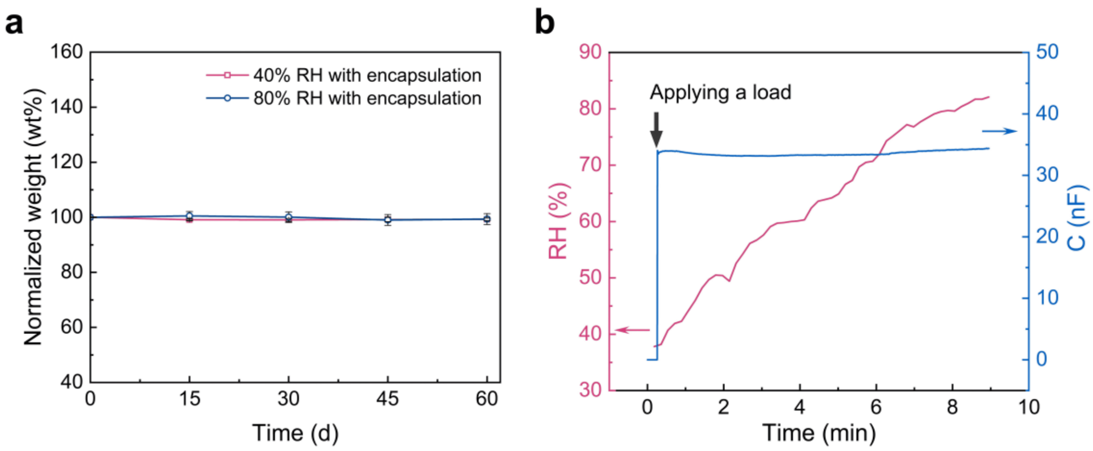

Supplementary Fig. 14. The hydration stability of encapsulated GSM biogel-based iontronic sensor. a, The normalized weight variation of encapsulated GSM biogel-based iontronic sensor under different humidity conditions (40% RH and 80% RH) for 60 days. b, The capacitance variation of the encapsulated GSM biogel-based iontronic sensor under fluctuating relative humidity (40–80% RH). Encapsulated GSM biogel-based iontronic sensor showed no measurable weight change after 60 days of storage under different humidity (40% RH and 80% RH), and the capacitance changed negligibly as the relative humidity fluctuated between 40% and 80%. These results confirmed that once equilibrated and properly encapsulated, the biogel-based iontronic sensor exhibits robust hydration stability suitable for reliable real-world sensing applications. Data were presented as mean values +/- SD, n=3.

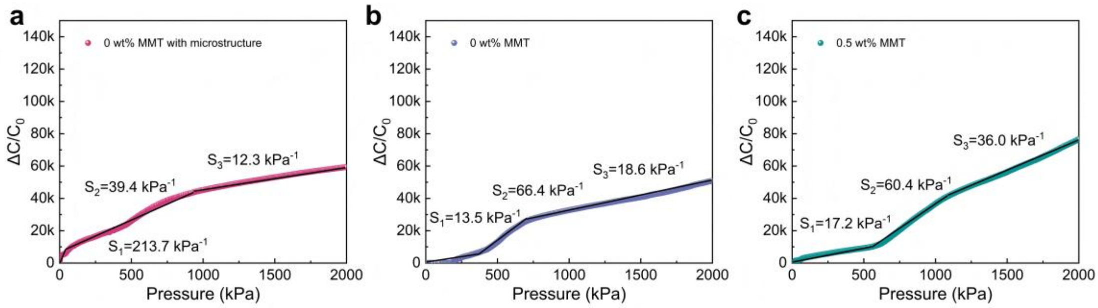

Supplementary Fig. 15. Relative capacitance change (*ΔC/C₀*) as a function of pressure among biogels-based iontronic sensors. a, 0 wt% MMT biogel with microstructure. b, 0 wt% MMT biogel without microstructure. c, 0.5 wt% MMT biogel without microstructure. These results demonstrated that both MMT and the microstructure contributed to enhancing the sensitivity.

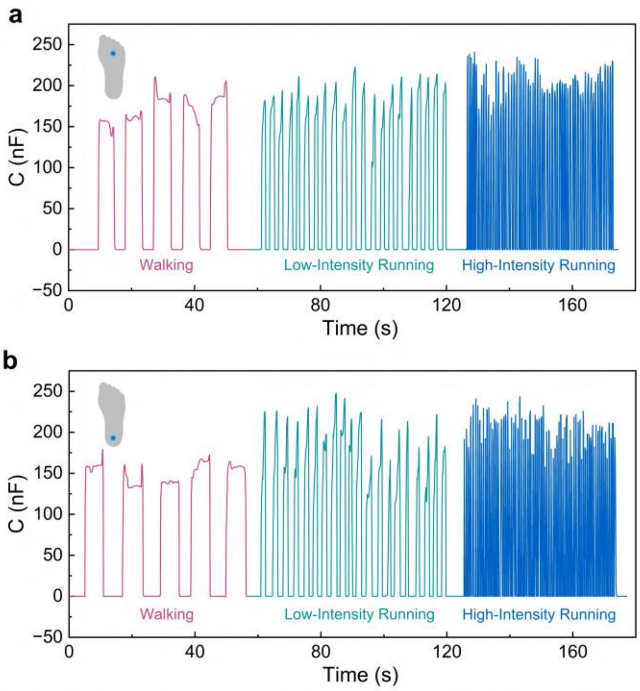

Supplementary Fig. 16. Capacitance variations of GSM biogel-based iontronic sensors placed on the soles of the feet during walking and running. a, Forefoot. b, Heel. These results showed that two sensors placed on the forefoot and heel successfully mapped the pressure distribution of the foot during different gait phases and demonstrated reliable performance under substantially higher loads.

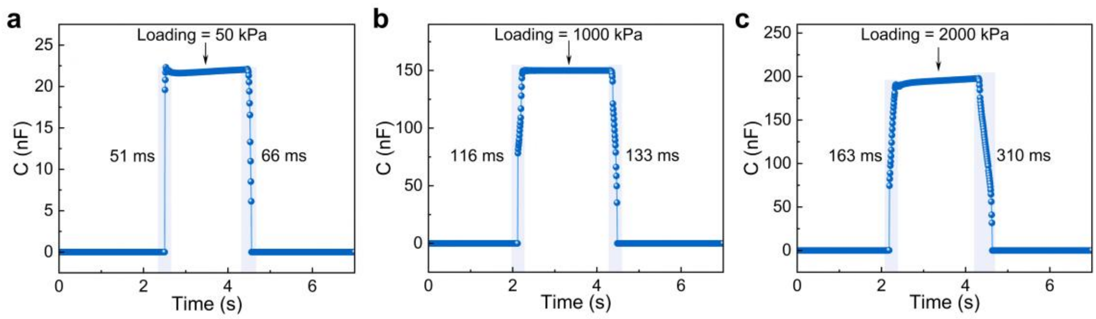

Supplementary Fig. 17. Response and recovery times of the iontronic sensor under different pressure. a, 50 kPa. b, 1000 kPa. c, 2000 kPa. It was found that both the response and recovery times became longer at higher pressures than at lower pressures. This trend could be attributed to the larger deformation imposed under high loads, which required a longer time for the hydrogel network to fully relax mechanically.

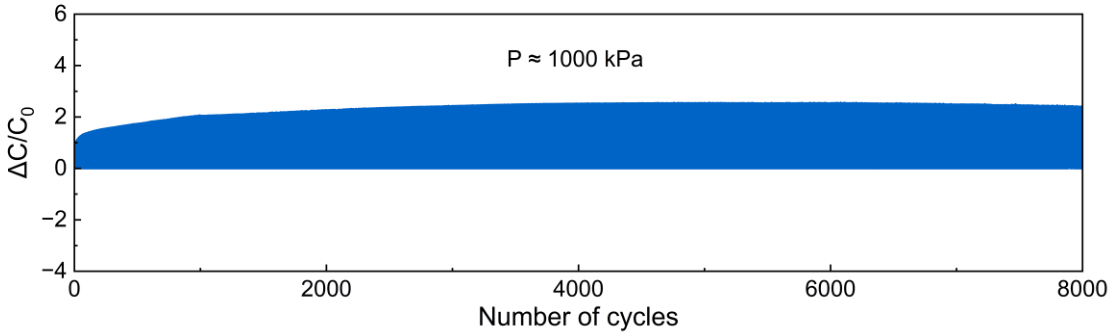

Supplementary Fig. 18. Cyclic compressive test of GSM biogel-based iontronic sensor over 8000 cycles at 1000 kPa at a frequency of 1 Hz. It was found that the capacitance change rate of the sensor gradually increased during the first 1000 cycles. This behavior was likely associated with the continuous dissociation and reformation of non-covalent interactions within the biogel network, which led to irreversible microstructural rearrangement and was reflected in gradual macroscopic changes, such as reduced thickness or increased contact area. After approximately 1000 cycles, the capacitance change rate became stable, indicating that the biogel network had reached a dynamically stable state and that no further cumulative geometric changes occurred. These results demonstrated cycling stability and long-term operational reliability of the sensor.

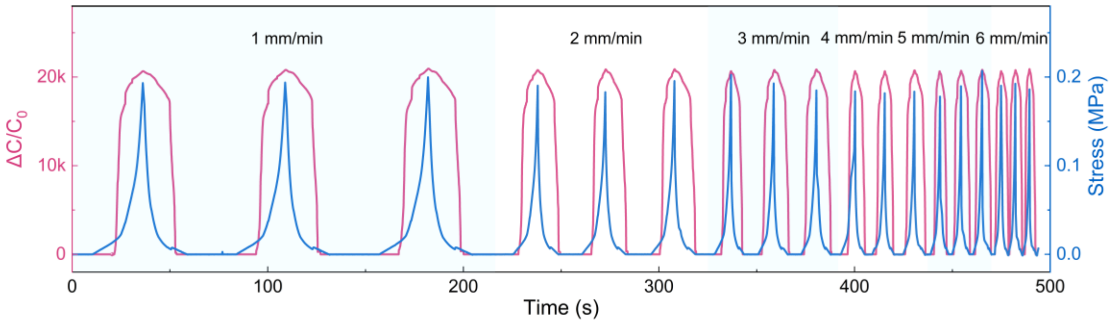

Supplementary Fig. 19. Capacitance variations at different loading speeds at 200 kPa. It was found that the iontronic sensor exhibited stable and continuous responses over a range of loading speeds from 1 to 6 mm min^{-1}, and the response rate of the iontronic sensor depended on the loading speeds.

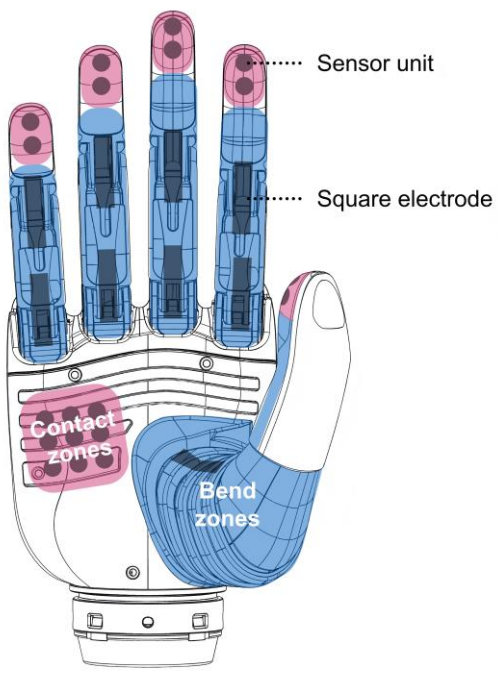

Supplementary Fig. 20. A schematic diagram of the functional divisions of the dexterous robotic hand. Both the electrode and sensor designs are specifically tailored to the anatomy of the dexterous robotic hand used in our experiments, whose fingers and palm can be divided into contact zones (fingertip pads and palm center) and bend zones (finger joints).

Supplementary Fig. 21. Schematic diagram of silver electrode screen printing. The electrodes were fabricated by screen printing silver paste through a 200-mesh screen onto a polyester fabric mesh coated with a photosensitive adhesive. This mesh was subsequently attached to a flexible TPU substrate 100 μm thick.

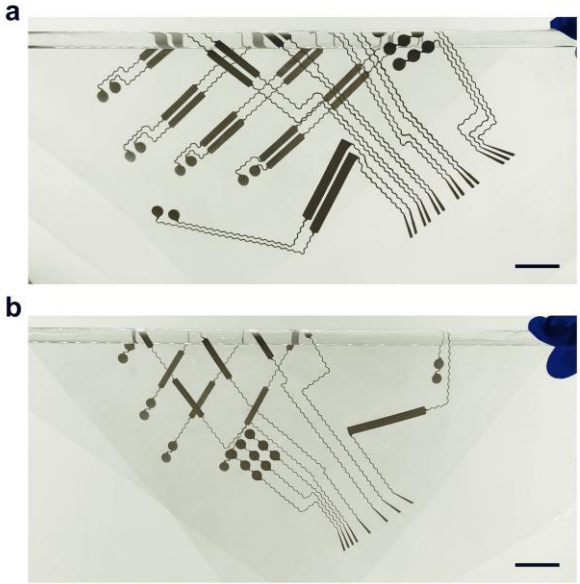

Supplementary Fig. 22. Photographs showing the flexible Ag/TPU electrodes. a, Photograph of the upper Ag/TPU electrodes. b, Photograph of the bottom Ag/TPU electrode. Scale bars, 2 cm.

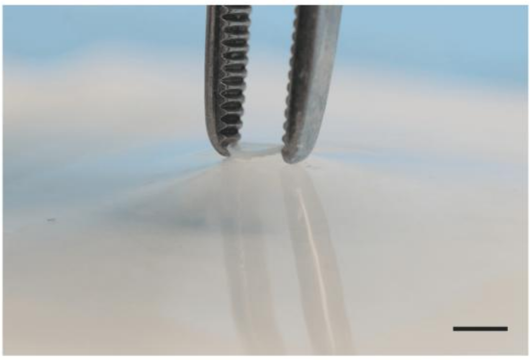

Supplementary Fig. 23. Photographs of PET disc adhering to TPU substrate after pulling. It was found that the PET disc exhibited strong adhesion to the TPU substrate. Scale bar, 1 cm.

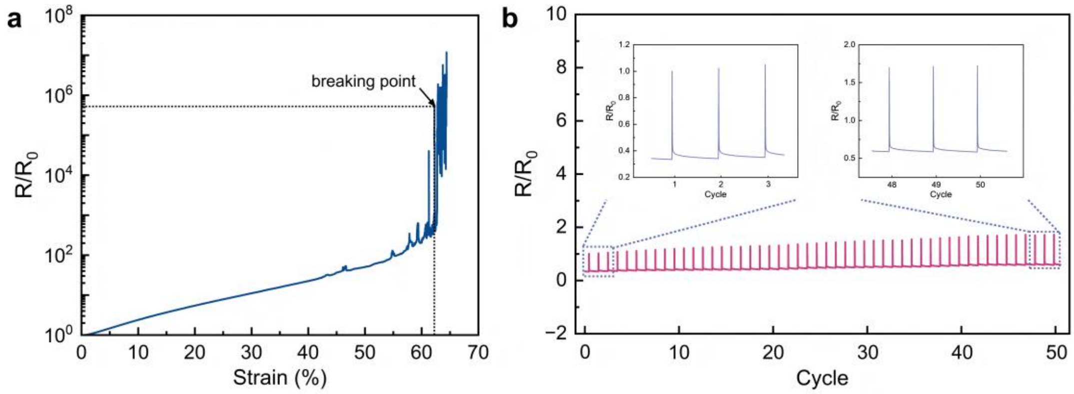

Supplementary Fig. 24. The resistance change of the Ag/TPU electrode under stretching. a, The electrical resistance of the Ag/TPU electrode changing with uniaxial strains. b, The electrical resistance of the Ag/TPU electrode changing at 10% uniaxial strain. These results demonstrated that the Ag/TPU electrode maintained electrical stability even when stretched to 60%, and exhibited relatively stable resistance changes under 50 cycles of 10% tensile strain.

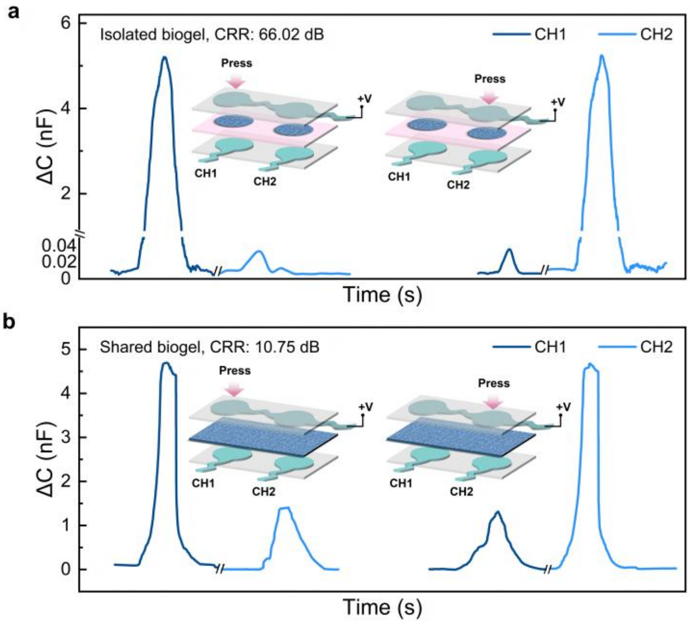

Supplementary Fig. 25. Cross-talk suppression through PDMS spacer design. a, Isolated biogel with PDMS spacer design demonstrated low cross-talk. b, Shared biogel without PDMS spacer design demonstrated high cross-talk. To quantify the crosstalk isolation performance, we evaluated the system using the Crosstalk Rejection Ratio (*CRR*), defined as $CRR = 20\ \log_{10}(\Delta C_{stressed}/\Delta C_{adjacent})$, where $\Delta C_{stressed}$ and $\Delta C_{adjacent}$ are the relative capacitance changes of the stressed central unit and the vertically adjacent units, respectively[1,2]. Take a 1×2 serpentine array as an example, in the isolated biogel with PDMS spacer, the *CRR* was 66.02 dB, while in the control sample the crosstalk phenomenon was very obvious, with 10.75 dB *CRR* observed. This indicated that PDMS spacer acts as a physical barrier between pixels, effectively preventing deformation from overflowing to adjacent pixels and ensuring that the pressure sensing signal mainly comes from the expected sensing unit.

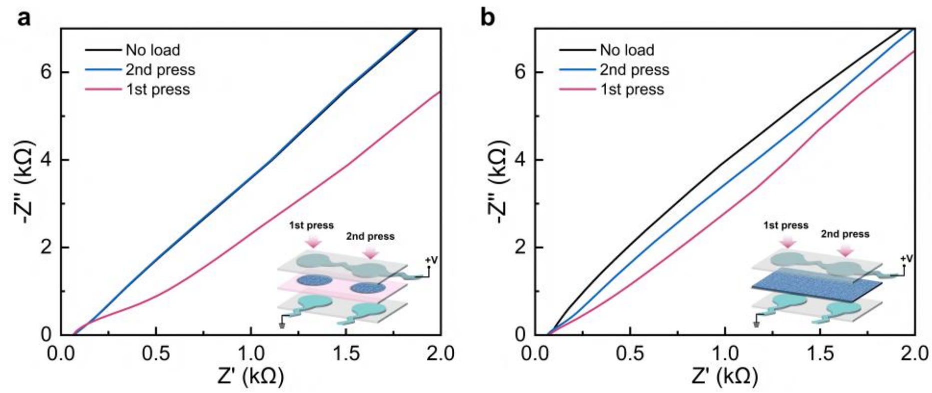

Supplementary Fig. 26. Nyquist plots of the two sensor configurations. a, Sensing elements of isolated biogel with PDMS spacer design. b, Sensing elements of shared biogel without PDMS spacer design. For the case using the PDMS spacer design, no change in signal of a target sensing element occurs when touching the neighboring sensing element because of no ion migration.

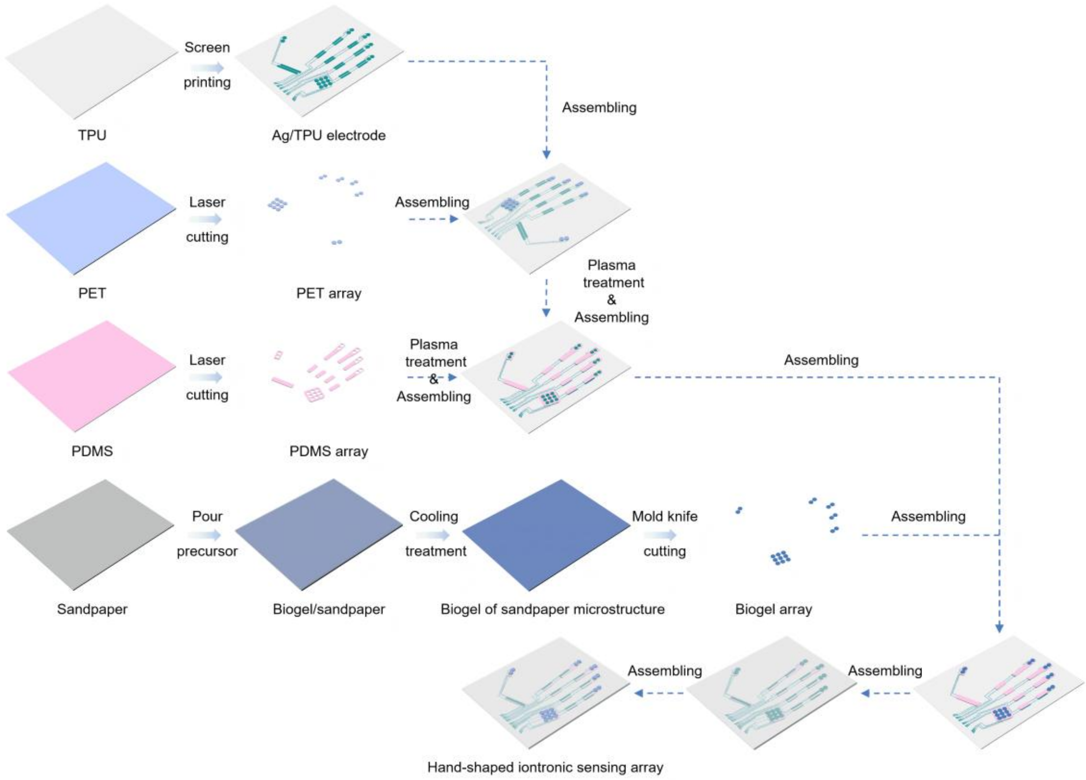

Supplementary Fig. 27. Schematic diagram of the hand-shaped iontronic sensor array assembly process. The schematic diagram illustrated the stepwise assembly process of the hand-shaped iontronic sensor array, including the fabrication of the Ag/TPU electrode, PET fixing discs, PDMS spacer, and microstructured biogel. Subsequently, plasma treatment and multi-layer assembly were performed to obtain the final hand-shaped iontronic sensing array.

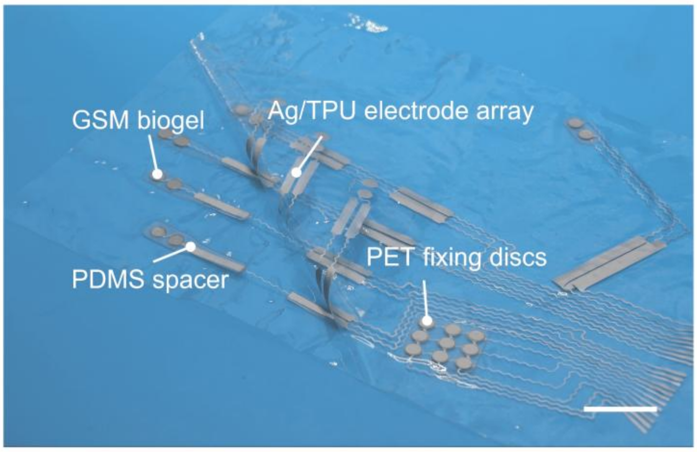

Supplementary Fig. 28. Photograph of the hand-shaped iontronic sensor array with a multi-layer structure. The hand-shaped iontronic sensor array consisted of the GSM biogels, Ag/TPU electrode arrays, PDMS spacers, and PET fixing discs. Scale bar, 2 cm.

a b

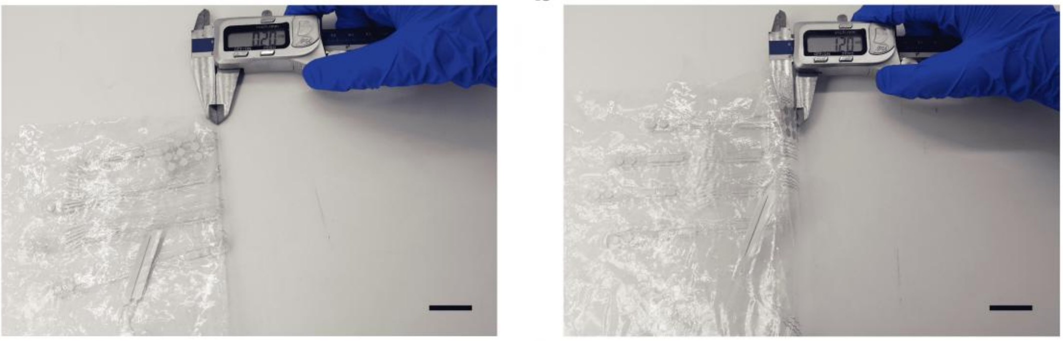

Supplementary Fig. 29. Photographs showing the ultra-thin hand-shaped iontronic sensor array. Photographs of the hand-shaped iontronic sensor array displaying a, the thinnest and b, the thickest parts. Scale bars, 2 cm.

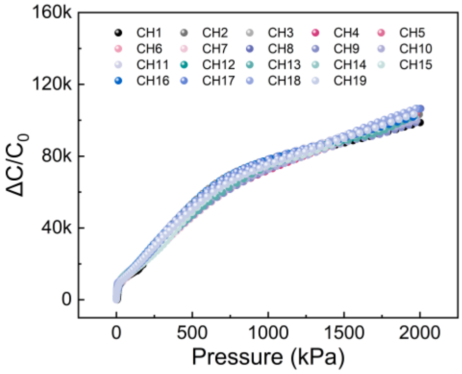

Supplementary Fig. 30. ***ΔC/C₀*** **as a function of pressure among all sensing units of the hand-shaped iontronic sensor array.** It was found that all 19 sensing units of the hand-shaped iontronic sensor array exhibited highly repeatable sensing performance across different sensing units, demonstrating fabrication reproducibility.

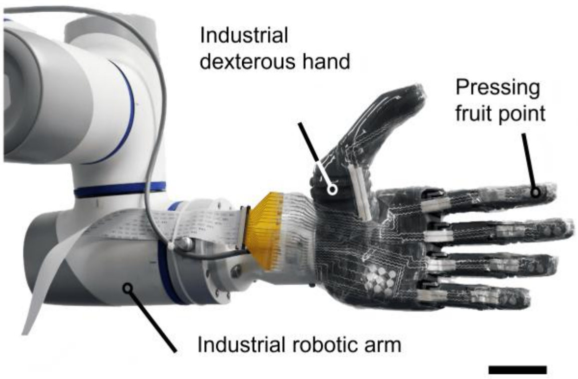

Supplementary Fig. 31. Photograph of the robotic system. The robotic system consisted of an industrial robotic arm and an industrial dexterous hand, which was assembled with the hand-shaped iontronic sensor array. Scale bar, 2 cm.

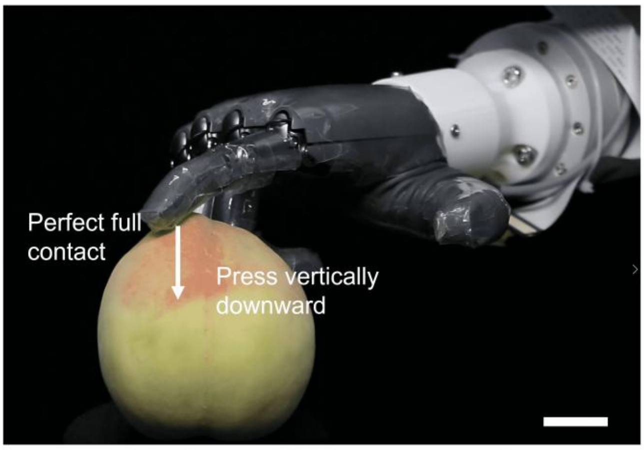

Supplementary Fig. 32. Photograph showing the dexterous hand assembled with the hand-shaped iontronic sensor array detecting the ripeness of fruits through single-channel signal acquisition. The index finger of the dexterous hand made perfect full contact with the peach surface, and then the robotic arm was controlled to move the dexterous hand vertically downward. Scale bar, 2 cm.

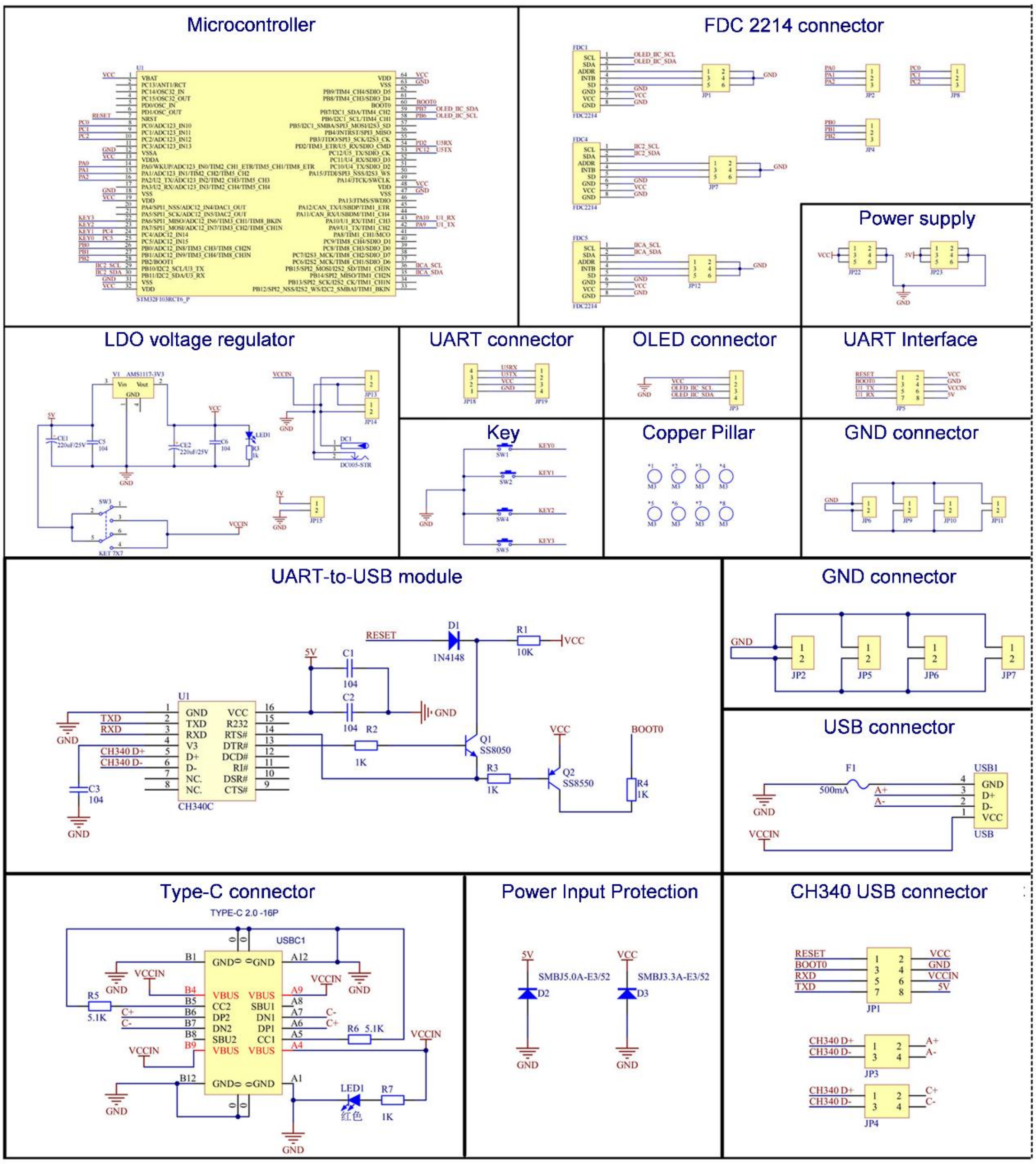

Supplementary Fig. 33. Schematic diagram of the circuit board.

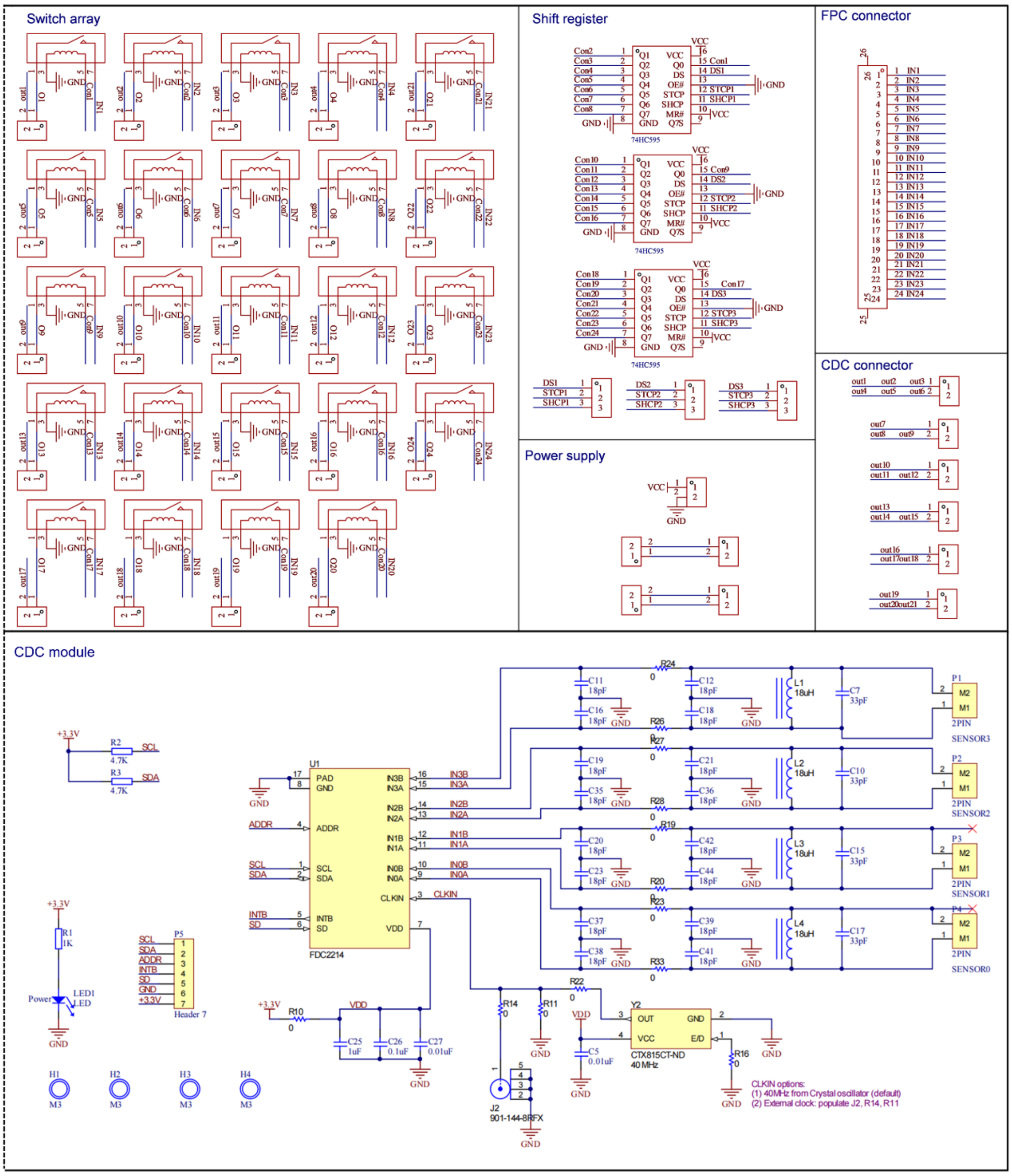

Supplementary Fig. 33 (Continued). Schematic diagram of the circuit board. This schematic diagram illustrated the full circuit design of a custom data acquisition system. The main control board included a microcontroller, LDO voltage regulators, a UART-to-USB module, and various connectors for power, communication, and user interaction. The sensor interface board featured a switch array, shift registers, an FDC2214 CDC module, and dedicated connectors for interfacing with the capacitive sensor array.

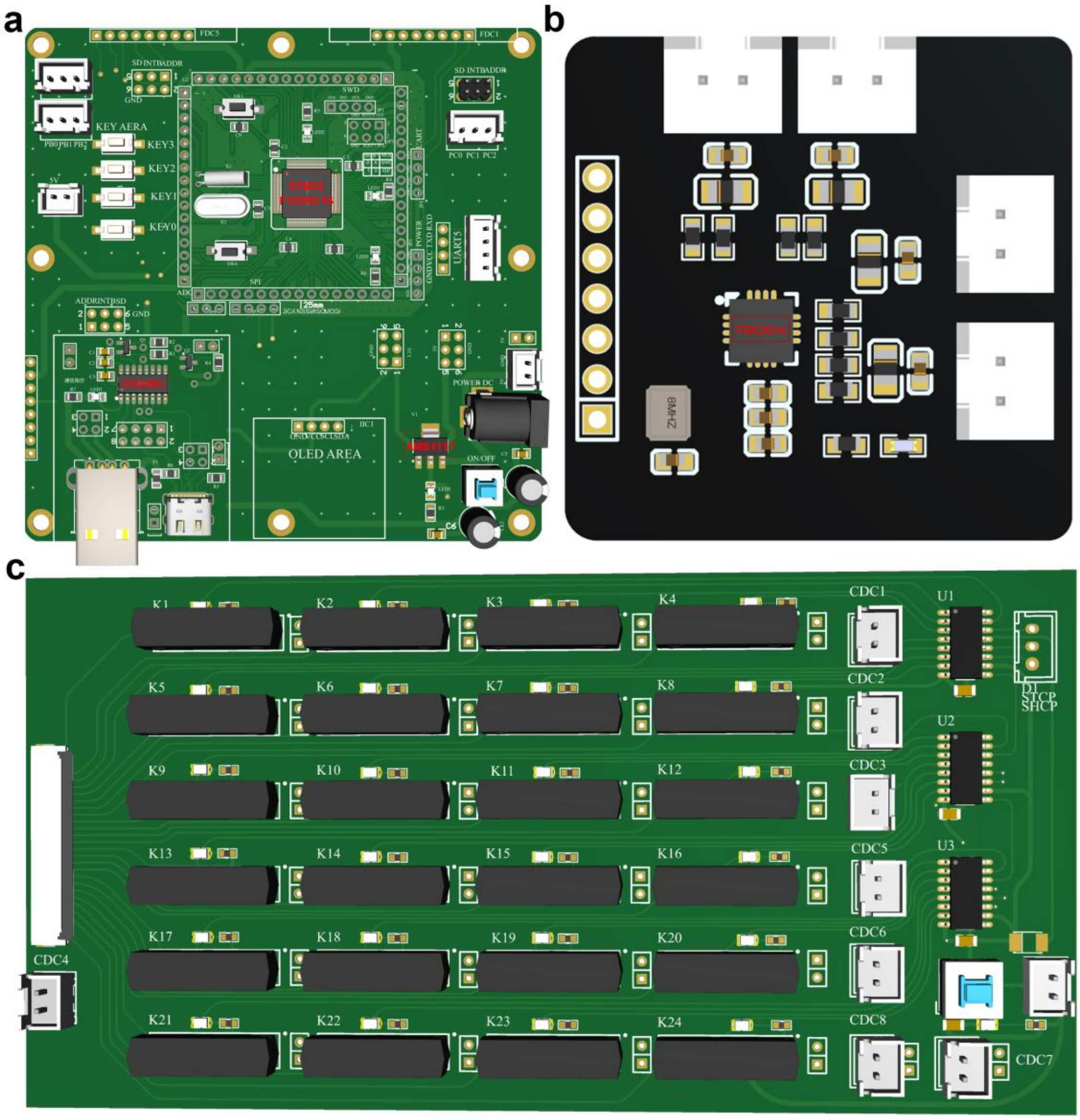

Supplementary Fig. 34. 3D model diagram of the circuit board. a, The main microcontroller module with control and communication interfaces. b, The 4-channel FDC2214 CDC modules. c, The multiplexer module designed to support 24 sensor channels for expanded signal acquisition.

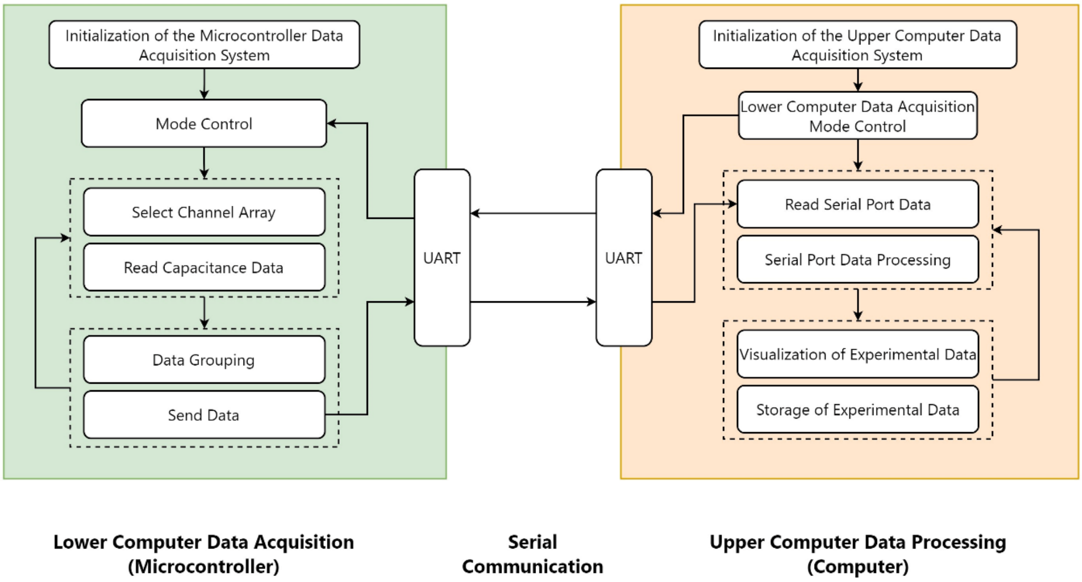

Supplementary Fig. 35. Schematic illustrations of the working principle of the data acquisition system. This schematic illustrated the working principle of a two-part data acquisition system, consisting of a lower-computer (microcontroller) unit for data collection and an upper-computer (computer) unit for data processing, which communicated with each other via UART serial communication.

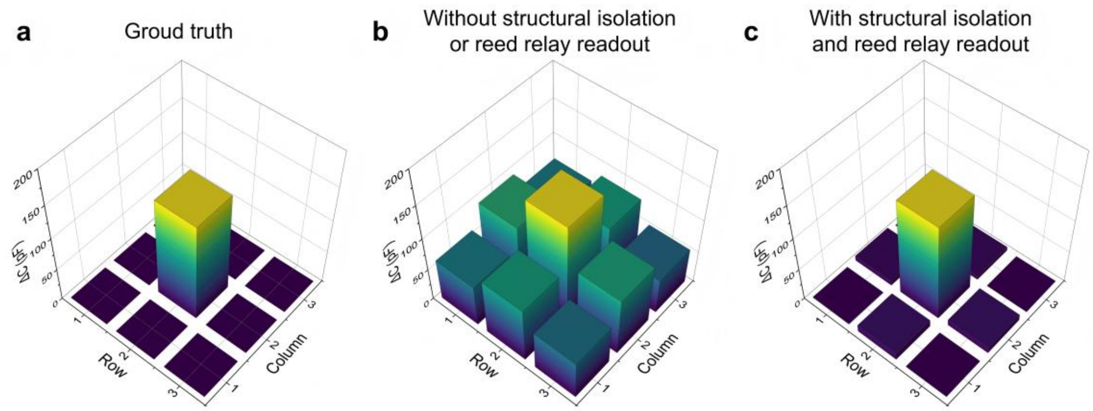

Supplementary Fig. 36. Crosstalk suppression of different 3×3 test arrays. a, Capacitance distribution of the test array with structural isolation as the ground truth measured using an LCR meter. b, Capacitance distribution of the test array without structural isolation measured using ADG734 semiconductor switch. c, Capacitance distribution of the test array with structural isolation measured using reed relays. The array without structural isolation or reed relay readout exhibited severe crosstalk, with an CRR of 7.26–10.45 dB. In contrast, the array incorporating both the structural design and the reed relay readout achieved a high CRR of 56.48–62.40 dB comparable to that of the structurally isolated benchmark, demonstrating that the relay circuit suppresses electrical crosstalk without compromising the mechanical isolation. These results confirmed that the synergistic integration of structural and circuit-level designs minimizes both mechanical and electrical crosstalk, ensuring reliable pressure sensing.

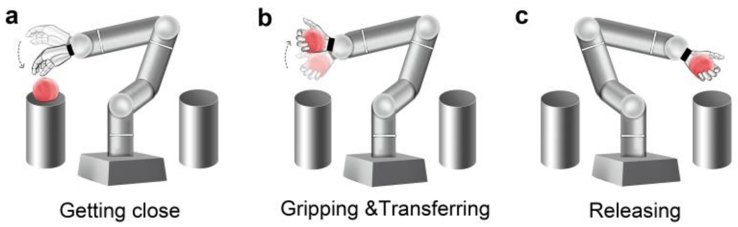

Supplementary Fig. 37. Schematic diagrams of the process of grasping fruits. a, Getting close. b, Gripping & Transferring. c, Releasing.

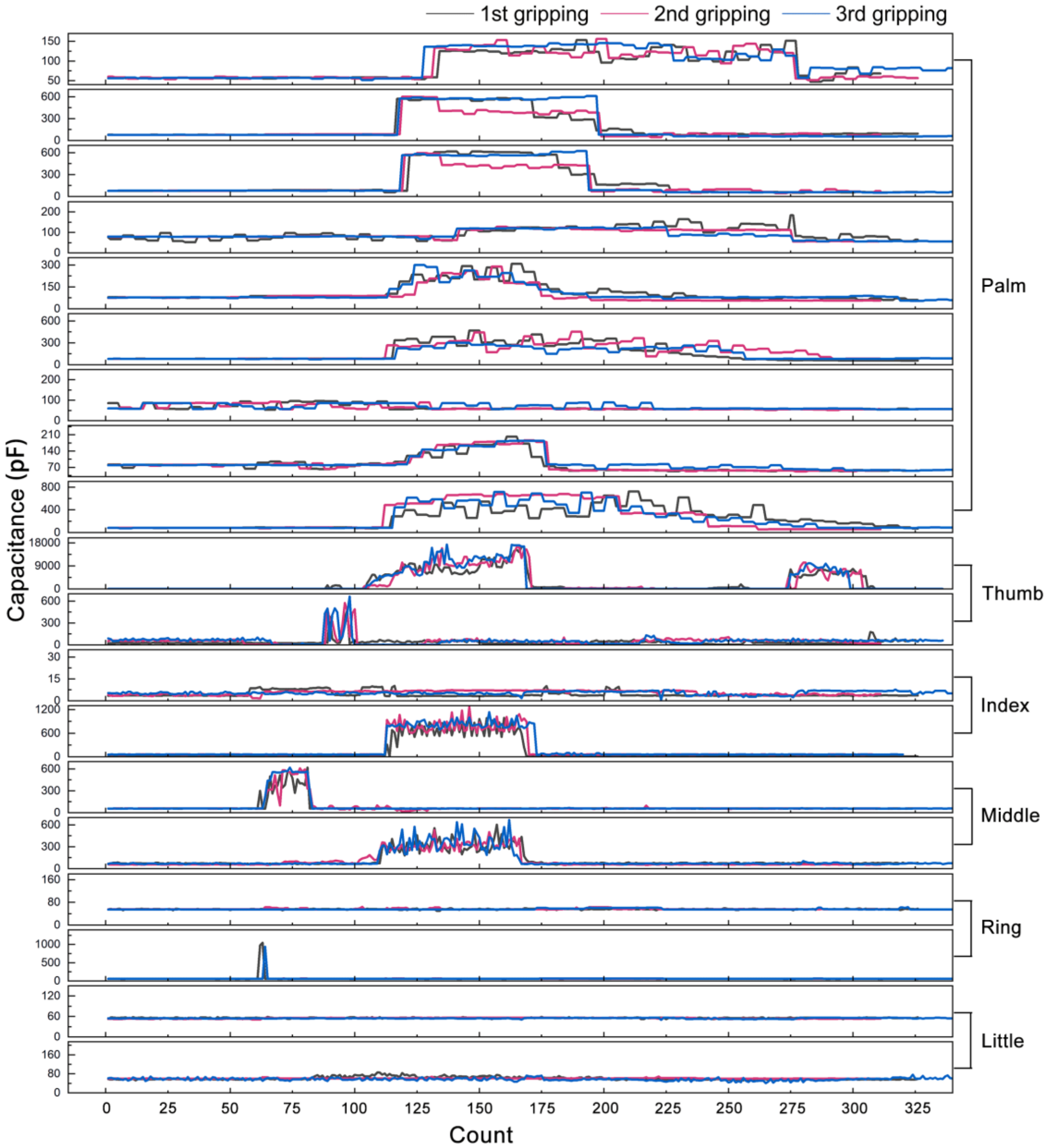

Supplementary Fig. 38. The capacitance value of all 19 sensing units in the hand-shaped sensor array during grasping the same peach. It was found that all 19 sensing units in the hand-shaped sensor array exhibited distinct and reproducible signal patterns corresponding to the pressure distribution generated during repeated grasping of the same peach. These results demonstrated that the complete sensor configuration maintains stable sensing performance during cyclic operation.

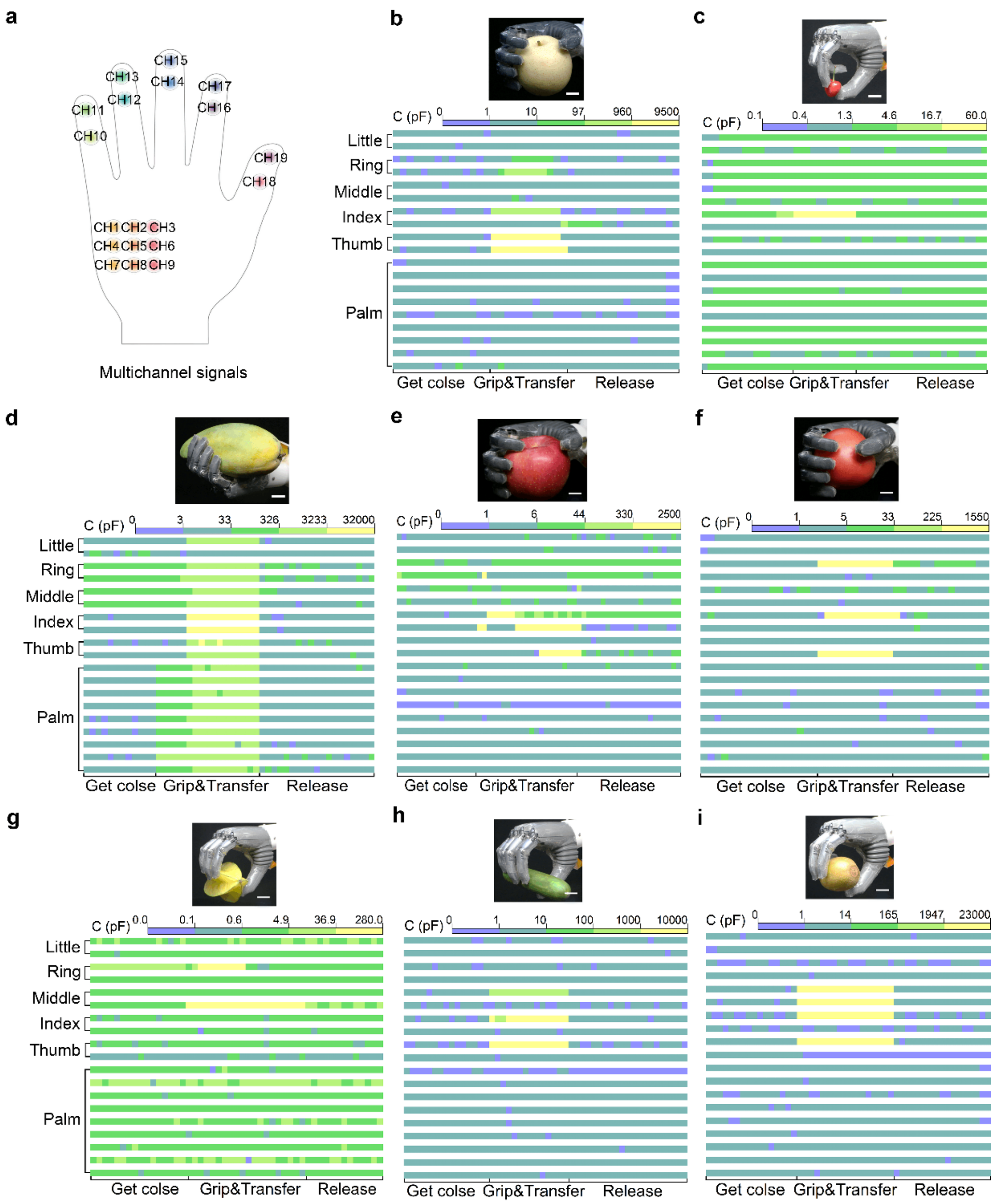

Supplementary Fig. 39. The capacitive signals of the process of grasping different fruits with different gestures. a, Schematic diagram of 19 sensing units in the hand-shaped sensor array. b-i, Photograph of grasping different fruits and the characteristic heat map of the capacitance response during the process of getting close-gripping and transferring-releasing. b, Pear. c, Cherry. d, Mango. e, Apple. f, Tomato. g, Carambola. h, Cucumber. i, Kiwi. Scale bars, 2 cm.

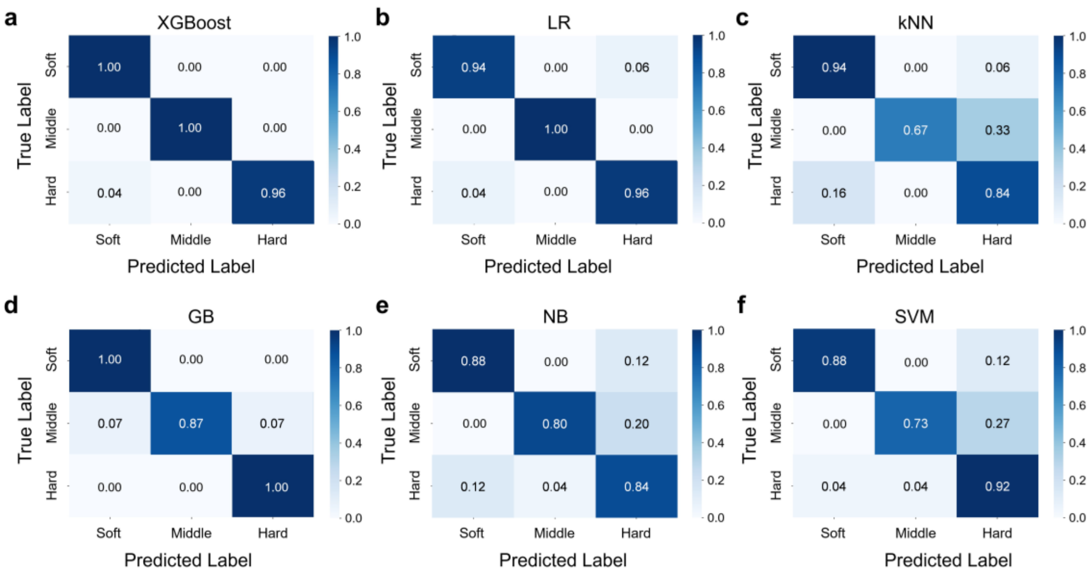

Supplementary Fig. 40. Confusion matrices of different supervised learning models on the fruit ripeness dataset. a, XGBoost. b, LR. c, kNN. d, GB. e, NB. f, SVM. These results demonstrated their classification performance across soft, middle, and hard categories.

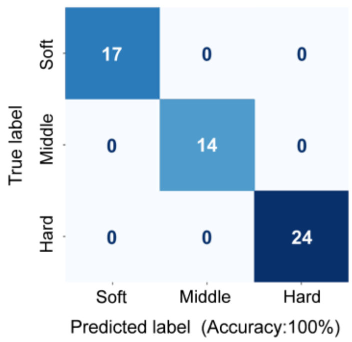

Supplementary Fig. 41. Confusion matric of TC-FRM on 55 independent external validation set. It was found that the model achieved a 100% prediction accuracy on the external validation set, showing its robust predictive performance.

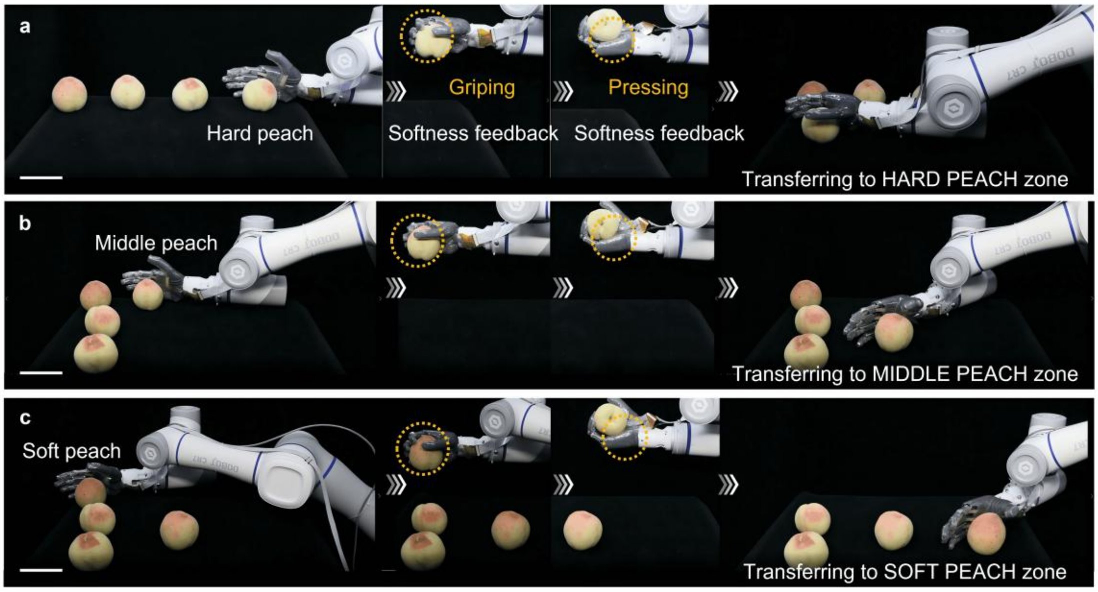

Supplementary Fig. 42. Photographs of the process of a dexterous hand assembled with the hand-shaped iontronic sensor array grasping peaches of unknown ripeness. a, Hard peach. b, Middle peach. c, Soft peach. The dexterous hand first approached the peach of unknown ripeness and then proceeded to grasp it. During grasping, contact between the peach and the sensing units generated characteristic capacitance curves. After obtaining the softness feedback, the dexterous hand placed the peach into a designated sorting area. Scale bars, 7 cm.

Supplementary Tables

Supplementary Table 1. Biogel recipes with varying compositions.

Sample	Gelatin	SL	MMT	Deionized Water
Gelatin hydrogel	1.5 g	0 g	0 mL	8.5 g
GS biogel	1.5 g	2 g	0 mL	6.5 g
GSM biogel	1.5 g	2 g	1 mL 5 wt%	5.5 g

Supplementary Table 2. GSM biogel recipes with varying MMT weight ratio.

Sample	Gelatin	SL	MMT	Deionized Water
1	1.5 g	2 g	0 mL	8.5 g
2	1.5 g	2 g	1 mL 0.1 wt%	6.5 g
3	1.5 g	2 g	1 mL 0.5 wt%	5.5 g
4	1.5 g	2 g	1 mL 1 wt%	5.5 g
5	1.5 g	2 g	1 mL 5 wt%	5.5 g
6	1.5 g	2 g	1 mL 10 wt%	5.5 g
7	1.5 g	2 g	1 mL 20 wt%	5.5 g

Supplementary Table 3. GS biogel recipes with varying SL weight ratio.

Sample	Gelatin	SL	MMT	Deionized Water
1	1.5 g	0 g	0 mL	8.5 g
2	1.5 g	1 g	0 mL	7.5 g
3	1.5 g	1.5 g	0 mL	7 g
4	1.5 g	2 g	0 mL	6.5 g
5	1.5 g	2.5 g	0 mL	6 g
6	1.5 g	3 g	0 mL	5.5 g

Supplementary Table 4. Material parameters for finite element simulation.

Material	Young modulus (MPa)	Poisson's ratio	Density (g mL^{-1})	Yield stress 1 （MPa）	Plastic strain 1	Yield stress 2 （MPa）	Plastic strain 2
GSM biogel	1.33	0.45	1.18	/	/	/	/
TPU	3.39	0.4	0.98	3.68	0	50	6
Ag	16.63	0.3	3.19	1	/	/	/
PDMS	19.48	0.3	1	3.16	0	5.37	3.92
PET	1168.89	0.3	1.28	77.12	/	/	/

Supplementary Table 5. Comparison of sensing performances between our sensor and other capacitive-type flexible pressure sensors based on microstructured soft materials.

Compositions	Microstructures	Sensitivity	Working range	Derived from nature	Ref
SBMA/DADMAC/PAM	Sandpaper microstructure	7.92 kPa^{-1}	1 Pa–10 kPa	No	*(3)*
PVDF-HFP/[EMIM][TFSI]	Leaf microstructure	54.3 kPa^{-1}	0.1 Pa–115 kPa	No	*(4)*
PVDF-HFP/[EMIM][TFSI]	Pyramid microstructure	4.5 kPa^{-1}	0.2 Pa–10 kPa	No	*(5)*
PVDF-HFP/[EMIM][TFSI]	Gradient micropyramid	33.7 kPa^{-1}	0.36 Pa–1700 kPa	No	*(6)*
PAM/SA/$CaCl_2$	Wrinkled	164 kPa^{-1}	Up to 44.3 kPa	No	*(7)*
PAM/Silk fibroin/LiBr	Stainless mesh microstructure	0.4 kPa^{-1}	12 Pa–45 kPa	No	*(8)*
PVA/H_3PO_4	Sandpaper microstructure	3302.9 kPa^{-1}	0.08 Pa–360 kPa	No	*(9)*
PVA/[EMIM][OTF]	Slant hierarchical	36000 kPa^{-1}	0.015 Pa –300 kPa	No	*(10)*
PVA/H_3PO_4	Graded hollow ball arch	10420.8 kPa^{-1}	0.2 Pa–300 kPa	No	*(11)*
PVA/H_3PO_4	Graded semiellipsoidal	49.1 kPa^{-1}	Up to 485 kPa	No	*(12)*
Gelatin/SL/MMT	**Sandpaper microstructure**	**466.3 kPa^{-1}**	**20 Pa–2000 kPa**	**Yes**	**This work**

Supplementary Table 6. The optimal hyperparameters of each model.

Model	Optimal Hyperparameters
RF	n_estimators=100, max_depth=10, min_samples_split=2, min_samples_leaf=1
SVM	C=10, kernel='poly', degree=2, gamma=0.001, coef0=0.5
GB	n_estimators=200, learning_rate=0.2, max_depth=1,
XGBoost	alpha=0.01, n_estimators=200, learning_rate=0.1, max_depth=3, colsample_bytree=0.1
LR	C=1.0, class weight='balanced, multi_class=‘ovr', penalty='l1', solver='liblinear'
kNN	n_neighbors=3, weights='uniform', metric='manhattan'
NB	Default parameters

Supplementary Table 7. The complete cross-validation results of each model.

Model	CV Score	Train Score	Test Accuracy
RF	0.9692	1	1
XGBoost	0.9615	1	0.9825
GB	0.9387	1	0.9649
kNN	0.8783	0.9545	0.8246
NB	0.8698	0.9924	0.8421
LR	0.8248	1	0.9649
SVM	0.7875	1	0.8596

Supplementary Table 8. Main hyperparameter search ranges for each model.

Model	Hyperparameter	Search Range/Values
RF	n_estimators	100, 200, 300
	max_depth	None, 5, 10, 20
	min_samples_split	2, 5, 10
	min_samples_leaf	1, 2, 3, 4
GB	n_estimators	100, 200, 300
	learning_rate	0.05, 0.1, 0.2
	max_depth	1, 3, 5
XGBoost	n_estimators	100, 200, 300
	learning_rate	0.05, 0.1, 0.2
	max_depth	1, 3, 5
	alpha	0.01, 0.1, 10, 20
	colsample_bytree	0.3, 0.5, 0.7
SVM	C	0.1, 1, 10, 1000
	kernel	'linear', 'rbf', 'poly', 'sigmoid'
	degree	2, 3, 4 (only for 'poly')
	coef0	0.0, 0.5, 1.0 (for 'poly'/'sigmoid')
	gamma	'scale', 'auto', 0.001, 0.01, 0.1
LR	C	0.1, 1, 10
	penalty	'l1', 'l2'
	solver	'liblinear', 'saga'
	class_weight	None, 'balanced'
kNN	n_neigbborse	3, 5, 7, 9
	weightse	'uniform', 'distance'
	metrice	'euclidean', 'anhattan', 'ninkoxski'
NB	–	No hyperparameter tuning

Supplementary References

1. Zhao, Y. C., Xu, W., Guo, W. C. & Sheng, X. J. Strain-insensitive, crosstalk-suppressed, ultrawide-linearity iontronic tactile skin from a synergistic segment-embedded strategy. *ACS Sens.* **10**, 6765-6774 (2025).
2. Li, Y. H., Long, J. Y., Chen, Y., Huang, Y. & Zhao, N. Crosstalk-free, high-resolution pressure sensor arrays enabled by high-throughput laser manufacturing. *Adv. Mater.* **34**, 9 (2022).
3. Liu, X., Ji, X. Y., Zhu, R. J., Gu, J. F. & Liang, J. J. A microphase-separated design toward an all-round ionic hydrogel with discriminable and anti-disturbance multisensory functions. *Adv. Mater.* **36**, 16 (2024).
4. Qiu, Z. G. et al. Ionic skin with biomimetic dielectric layer templated from Calathea Zebrine leaf. *Adv. Funct. Mater.* **28**, 9 (2018).
5. Su, Q. et al. A stretchable and strain-unperturbed pressure sensor for motion interference-free tactile monitoring on skins. *Sci. Adv.* **7**, 9 (2021).
6. Yang, R. et al. Iontronic pressure sensor with high sensitivity over ultra-broad linear range enabled by laser-induced gradient micro-pyramids. *Nat. Commun.* **14**, 2907 (2023).
7. Zhou, S. et al. Multidimensional biomimetic construction of highly sensitive wrinkled gels based on the transformation of multiple supramolecular interactions induced by dual-solvent strategy. *Adv. Funct. Mater.* **34**, 15 (2023).
8. Li, S. et al. A skin-like pressure- and vibration-sensitive tactile sensor based on polyacrylamide/silk fibroin elastomer. *Adv. Funct. Mater.* **32**, 8 (2022).
9. Bai, N. N. et al. Graded intrafillable architecture-based iontronic pressure sensor with ultra-broad-range high sensitivity. *Nat. Commun.* **11**, 9 (2020).
10. Luo, Y. S. et al. Gecko-inspired slant hierarchical microstructure-based ultrasensitive iontronic pressure sensor for intelligent interaction. *Research* **2022**, 13 (2022).
11. Ding, Z. et al. Highly sensitive iontronic pressure sensor with side-by-side package based on alveoli and arch structure. *Adv. Sci.* **11**, 11 (2024).
12. Bai, N. N. et al. Graded interlocks for iontronic pressure sensors with high sensitivity and high linearity over a broad range. *ACS Nano* **16**, 4338-4347 (2022).